POLITECNICO DI TORINO
Repository ISTITUZIONALE

A low-power mixed-signal ASIC for readout of SiPM at cryogenic temperature

Original
A low-power mixed-signal ASIC for readout of SiPM at cryogenic temperature / Kugathasan, R.. - 370:(2020). (TWEPP Santiago de Compostela).

Availability:
This version is available at: 11583/2809354 since: 2020-04-07T10:20:44Z

Publisher:
Sissa Medialab srl

Published
DOI:

Terms of use:

This article is made available under terms and conditions as specified in the corresponding bibliographic description in the repository

Publisher copyright

(Article begins on next page)

18 November 2026

metals

MDPI

Article

Effect of PBF-LB/M Processing on the Microstructural Evolution and Local Mechanical Properties of Novel Al-Fe-Si-Cr-Ni Alloy

Alessandra Martucci *, Paolo Fino and Mariangela Lombardi *

Department of Applied Science and Technology, Politecnico di Torino, Corso Duca Degli Abruzzi 24, 10129 Turin, Italy; paolo.fino@polito.it

* Correspondence: alessandra.martucci@polito.it (A.M.); mariangela.lombardi@polito.it (M.L.)

Abstract: The present study aims to investigate the microstructural evolution and local mechanical properties of an AlFe18Si8Cr5Ni2 alloy processed via Powder Bed Fusion–Laser-Based Manufacturing (PBF-LB/M). Designed with a focus on sustainability, this alloy was produced by deriving the necessary elements from AlSi10Mg and 304L steel, two of the most widely used alloys and, consequently, among the easiest materials to source from machining scrap. By leveraging iron, chromium, and nickel from these widespread standard compositions, the alloy mitigates the detrimental effects of Fe contamination in Al-based alloys while simultaneously enhancing mechanical performance. A comprehensive investigation of the impact of rapid solidification and thermal cycling offered novel insights into phase stability, elemental distribution, and local mechanical behavior. In particular, microstructural analyses using scanning electron microscopy (SEM), field emission SEM, energy-dispersive X-ray spectroscopy, X-ray diffraction, and differential scanning calorimetry revealed significant phase modifications post PBF-LB/M processing, including Fe-rich acicular phase segregation at melt pool boundaries and enhanced strengthening phase formation. In addition, nanoindentation mapping was used to demonstrate the correlation between microstructural heterogeneity and local mechanical properties. The findings contribute to a deeper understanding of Al-Fe-Si-Cr-Ni alloy changes after the interaction with the laser, supporting the development of high-performance, sustainable Al-based materials for PBF-LB/M applications.

Keywords: Al-Fe-Si-Cr-Ni alloy; PBF-LB/M; powder bulk comparison; microstructural analyses; nanoindentation

check for updates

Academic Editors: Aman Gupta and Gyan Shankar

Received: 30 April 2025
Revised: 11 June 2025
Accepted: 12 June 2025
Published: 13 June 2025

Citation: Martucci, A.; Fino, P.; Lombardi, M. Effect of PBF-LB/M Processing on the Microstructural Evolution and Local Mechanical Properties of Novel Al-Fe-Si-Cr-Ni Alloy. *Metals* **2025**, *15*, 661. https://doi.org/10.3390/met15060661

Copyright: © 2025 by the authors. Licensee MDPI, Basel, Switzerland. This article is an open access article distributed under the terms and conditions of the Creative Commons Attribution (CC BY) license (https://creativecommons.org/licenses/by/4.0/).

1. Introduction

The development of novel Al-Si-Fe-based alloys has gained significant attention in recent years, driven by the urgent need to tackle the challenges posed by iron contamination in Al-Si alloys, particularly from a sustainability perspective [1,2]. The significance of this topic lies in the fact that Al-Si alloys, with their good specific mechanical properties, low density, good castability, and high corrosion resistance, are crucial in industries like automotive and aerospace [3]. However, the recycling of these alloys is often complicated by the presence of unavoidable iron impurities, which, even in small amounts, can lead to the formation of brittle intermetallic phases like Al_5FeSi (β) [4]. These phases significantly degrade mechanical properties and corrosion resistance, posing a significant barrier to the efficient recycling of Al-Si alloys.

In response to this challenge, recent research has focused on the development of Al-Fe-Si alloys containing additional elements, such as chromium, nickel, and manganese, which have been shown to act as effective iron correctors. Among the iron correctors, Cr, Ni, and Mn stand out for their ability to refine the morphology and distribution of iron-containing phases, thereby enhancing the overall mechanical performance of the alloy [5]. Cr, for instance, enhances the high-temperature strength by precipitating intermetallic phases that serve as inoculants [6]. At the same time, Ni contributes to the stabilization of mechanical properties at elevated temperatures and improves corrosion resistance [7,8]. The addition of Mn, on the other hand, has been demonstrated to induce a reduction in the size of the Al_5FeSi damaging phase by more than half [9]. The incorporation of these elements in higher concentrations is facilitated by rapid solidification processes, which can extend the solubility limits of alloying elements within the aluminum matrix [10]. This advantage can be leveraged in both the production of alloy powders and the fabrication of bulk materials. A previous study conducted by the authors has laid the groundwork by designing novel Al-Fe-Si-Cr-Ni compositions tailored for rapid solidification [11]. In that study, inert gas atomization (IGA) was used to create the novel AlFe18Si8Cr5Ni2, exploiting the rapid atomization cooling rate to increase the solubility limits of alloying elements, allowing for the creation of more complex and alloy-rich compositions.

Rapid solidification can offer significant advantages not only in the production of alloy powders but also in the fabrication of bulk components. The use of powders obtained through rapid solidification as a raw material of a manufacturing process that takes advantage of high cooling rates to further increase solubility limits and allow for the formation of microstructural features unreachable by traditional processes can be an effective method for designing never-before-explored compositions with unique mechanical properties [12]. Additive manufacturing (AM) technologies, particularly powder-based methods, such as Powder Bed Fusion–Laser-Based for Metals (PBF-LB/M), are ideally suited for exploiting these benefits. These technologies allow for layer by layer construction of bulk components, preserving and even amplifying the microstructural advantages introduced during rapid solidification [13]. Specifically, the PBF-LB/M process produces fine, homogeneously distributed microstructures, reduces the occurrence of defects, and facilitates the formation of desirable phases that improve strength, toughness, and thermal stability [14].

To understand the effect of the laser–powder interaction involved in the PBF-LB/M process on microstructural features and local mechanical properties, this research delved into the microstructural evolution of the composition before and after the additive process. In particular, by conducting advanced microstructural analyses with scanning electron microscopy (SEM) and field emission–SEM (FESEM), exploiting different detectors, phase identification by analyzing X-ray diffraction (XRD) patterns and thermal analyses with differential scanning calorimetry (DSC), it was possible to explore how laser scanning affects the solidification mechanisms and the phase formation in the PBF-processed AlFe18Si8Cr5Ni2. In addition, a preliminary micromechanical–microstructural correlation analysis was conducted by realizing a high-resolution nano-hardness map. The load–displacement curves obtained from each indentation were then thoroughly analyzed to extract mechanical parameters useful for predicting the macroscopic mechanical properties of the material.

2. Materials and Methods

2.1. Powder Feedstock

The AlFe18Si8Cr5Ni2 alloy powder was produced by our research group using a closed IGA process and by blending AISI 304L stainless steel and AlSi10Mg aluminum alloy ingots in a 1:8 ratio. All details of the atomization process can be found in the

previous work [11]. Before further characterizations, the powder was sieved between 20 and 63 μm, as suggested for PBF-LB/M production, in a lab-scale machine and dried at 80 °C for 2 h to remove the surface moisture. The particle size distribution was measured using a Mastersizer3000 laser diffraction particle size analyzer (Malvern Panalytical, Malvern, UK). In particular, the particles were characterized by D10, D50, and D90 values of 20.3, 31.8, and 50.2 μm, respectively. In addition, the SEM investigation performed with a Phenom ProX G6 (Thermo Fisher Scientific, Waltham, MA, USA) revealed that the particles predominantly exhibited a spherical morphology, which is ideal for powder bed applications, with a limited number of satellites attached to the main particles and minimal internal porosity. After an accurate image analysis on 20 images of cross-sectioned particles, the internal porosity was calculated to be around 0.08%. This value ensures no adverse effect on the processability of the powder during PBF-LB/M or the final level of densification in bulk samples.

2.2. PBF-LB/M Production

The entire PBF-LB/M production process was performed using a Print Sharp 250 (Sodick Co., Ltd., Yokohama, Japan) equipped with a single-mode fiber laser source in IR with a maximum power of 500 W, a wavelength of 1070 nm, and a laser spot size of 50 μm. Argon was employed as protective atmosphere during production. The system featured a build volume of 258 × 258 × 330 mm^3, providing adequate space for bulk sample fabrication.

To preliminarily investigate the laser–powder interaction during the PBF-LB/M process, the single scan track (SST) method was employed. This approach was initially exploited to easily and quickly analyze the effect of different process parameters on laser–powder interaction. Based on the results of the combined analyses on on-top and cross-sectioned SSTs, cubic samples with dimensions of 10 × 10 × 5 mm^3 were produced. The layer thickness was set at 30 μm, as recommended for Al-based alloys by the PBF-LB/M machine supplier. A scanning strategy with stripes with 67° counterclockwise rotations between consecutive layers was adopted for bulk production. This strategy was chosen for its effectiveness in minimizing residual stresses and promoting a more isotropic stress distribution within the component after the PBF-LB/M process [15]. In addition, platform preheating set at 100 °C was adopted for the entire job duration as a strategy to reduce thermal gradients and mitigate residual stresses. The complete set of process parameters used for the PBF-LB/M production of AlFe18Si8Cr5Ni2 alloy is reported in Table 1.

Table 1. PBF-LB/M process parameters.

Power (W)	Scanning Speed (mm/s)	Hatch Distance (μm)	Layer Thickness (μm)	Scanning Strategy	Platform Temperature (°C)
200	800	180	30	Standard 67°	100

After bulk production, all specimens were removed from the platform using an electrical discharge machine. The post-PBF-LB/M processing chemical composition of the material was determined through ICP analysis and is presented in Table 2.

Table 2. Chemical composition of AlFe18Si8Cr5Ni2 alloy processed through PBF-LB/M, as determined through ICP analysis.

Element Composition (wt.%)	Fe	Si	Cr	Ni	Mn	Al
PBFed AlFe18Si8Cr5Ni2	18.3	7.54	5.51	2.44	0.73	Bal

2.3. Characterizations

Microstructural characterization was performed on cross-sectioned AlFe18Si8Cr5Ni2 powder, SST cross-section, and bulk sample cut parallel to the build direction. Cross-sectioned powder and cut bulk samples were embedded in conductive resin and subjected to metallographic preparation to achieve a mirror-like surface finish before the microstructural analyses with SEM and FESEM. SEM analyses were performed with a back-scattered electron detector operating at a voltage of 15 kV to distinguish compositional variations based on differences in atomic weight between the elements. Additionally, microchemical analyses using an X-ray spectroscopy (EDS) detector were carried out to investigate phase morphology and distribution in depth. For high-magnification microstructural characterization, a Zeiss Merlin FESEM (Carl Zeiss S.p.a., Oberkochen, Germany) was employed. These analyses enabled the detailed observation of fine microstructural features, including phase morphologies, interphase boundaries, and secondary phase distributions, of the powder and bulk sample.

XRD analyses were conducted for phase identification at 40 kV and 40 mA with a X'Pert Powder XRD machine (Malvern Panalytical, Malvern, UK) using CuKα radiation in a Bragg–Brentano configuration. The data were collected over a 2θ range of 20 to 90° with a fine step size of 0.013° and a counting time of 45 s per step to ensure high-resolution results. Phase identification was carried out using HighScore software (developed by Malvern Panalytical, version 5.3a) to interpret the XRD spectra accurately. To further understand the thermal behavior and reaction sequences of the AlFe18Si8Cr5Ni2 powder and bulk sample, DSC analysis was performed using the NETZSCH DSC 214 Polyma instrument (NETZSCH Group, Waldkraiburg, Germany). DSC tests were conducted by setting a heating rate of 10 °C/min from 20 to 1400 °C, followed by a cooling phase at a rate of 20 °C/min. An Al_2O_3 crucible was used in combination with a protective argon atmosphere to ensure thermal stability and prevent oxidation during the test.

Finally, in accordance with the ISO 14577 standard [16], nanoindentation hardness tests were conducted on the bulk sample using a load-controlled method. A Bruker triboindenter Ti 950 (Bruker Corporation, Billerica, MA, USA) equipped with a Berkovich tip was employed for this purpose. A peak load of 7000 μN was applied, with a holding time of 2 s at the peak load. A total of 400 indents were performed in a 20 × 20 matrix, ensuring 10 μm spacing between indentations to prevent plastic deformation overlap between adjacent indents. The test procedure was fully automated, allowing for precise control over sample positioning, loading, holding, unloading, retraction, and movement to the next indentation point. The loading and unloading rates were set at 5 mN/s, and the peak load was held for 5 s before acquiring all load–depth curves. A minimal thermal drift of 0.10 nm/s was maintained throughout the tests to minimize experimental error. From the experimental data resulting in load–displacement (P–h) curves, it was possible to extract hardness (H) and the reduced Young's modulus (E_r) values based on the half-space elastic deformation theory using the Oliver and Pharr method [17]. By referring to the characteristics of the indenter and applying Equation (1), it was then possible to calculate the Young's modulus (E) of the analyzed material.

$$E_r = \left(\frac{1-\nu^2}{E} + \frac{1-{\nu_i}^2}{E_i}\right)^{-1} \quad (1)$$

where E_i is the elastic modulus of the indenter, ν_i is its Poisson's ratio, and ν is the Poisson's ratio of the sample approximated at 3. In this study, E_i is 1040 GPa and ν_i is 0.07.

Based on the load–displacement curves acquired from nanoindentation, the plasticity index (Ψ) can be calculated based on Equation (2) to evaluate the material deformation behavior [18]. Ψ offers valuable insight into the balance between elastic and non-elastic

deformation mechanisms within the material. This index effectively characterizes the material tendency to undergo permanent deformation under applied stress, thus providing a useful measure of its plastic-to-elastic response ratio during mechanical loading.

$$\Psi = \frac{h_r}{h_m} \quad (2)$$

where h_m is the maximum indentation depth and h_e is the elastic reversible indentation depth.

The hold segment at constant load, applied during the nanoindentation tests, was analyzed to capture the progressive increase in indentation displacement observed in each indentation. This displacement change is indicative of the material creep behavior, as creep manifests as time-dependent deformation under constant load [19]. By evaluating the evolution of displacement over time during the hold phase, the average creep rate ($\dot{\varepsilon}$) of the material was estimated using Equation (3).

$$\dot{\varepsilon} = \frac{1}{h}\frac{dh}{dt} \quad (3)$$

3. Results

3.1. Laser Effect on Microstructural Features

The microstructure of the powders produced via the IGA process has already been comprehensively analyzed, as detailed in [11]. In the present study, powder characterization was used as a comparative baseline to assess the microstructural evolution induced by PBF-LB/M. As shown in Figure 1, the cross-sectional analysis of an AlFe18Si8Cr5Ni2 powder particle, performed using Backscattered Electron (BSE) imaging and EDS, reveals the presence of three distinct phases. In particular, EDS mapping identifies Fe-rich regions, Si primarily segregated in Fe-depleted areas with isolated zones of nearly pure Si, and Cr-enriched areas that overlap with Si and Ni, suggesting the formation of complex intermetallic phases involving these three elements.

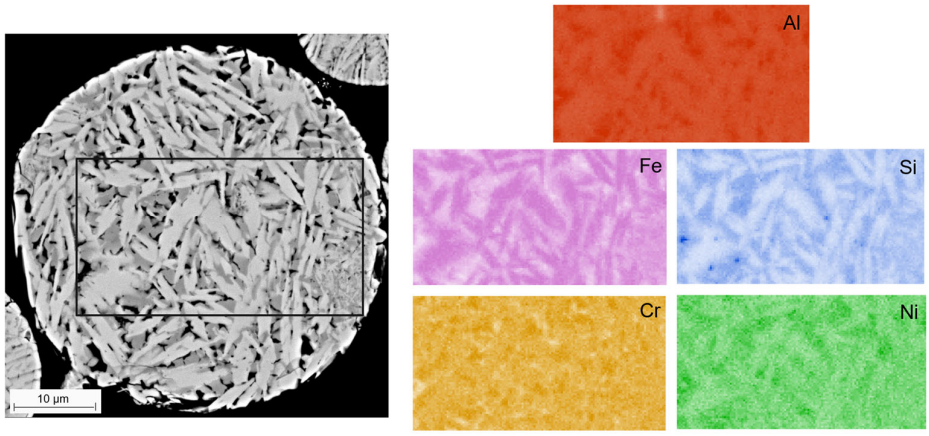


Figure 1. Cross-sectional SEM-EDS maps showing the spatial distribution of Al, Fe, Si, Cr, and Ni within AlFe18Si8Cr5Ni2 powder.

The rapid solidification during IGA resulted in a fine microstructure with well-dispersed phases and minimal segregation. The subsequent laser melting stage in PBF-LB/M is expected to alter the phase distribution, morphology, and chemical homogeneity due to localized melting, rapid cooling, and potential element redistribution.

To preliminarily investigate the effect of laser processing, the study began by analyzing the microstructure and elemental distribution within the SST cross-section to examine the effect of laser–powder interaction without the complexities associated with the thermal cycles of full-scale PBF-LB/M production. EDS analyses of the SST cross-sections revealed

how the alloying elements interacted under laser exposure. Figure 2 shows EDS maps of a representative SST cross-section, highlighting the distribution of the Al matrix and the two most abundant elements in the alloy, Fe and Si.

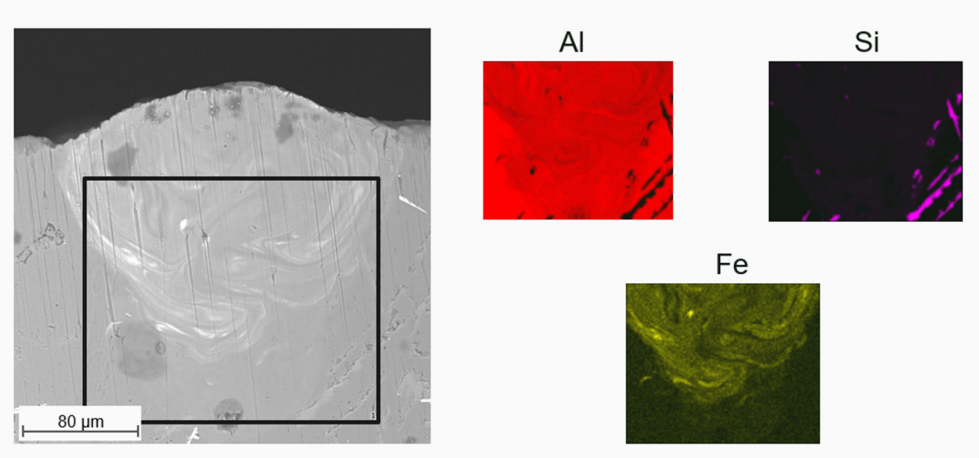


Figure 2. A representative BSE micrograph of the AlFe18Si8Cr5Ni2 SST cross-section and Al, Si, and Fe distribution maps obtained via EDS analysis.

The distribution of Si coincides with areas where Al is detected, while the large acicular features observed correspond to the platform material, which is composed of AlSi10Mg processed via casting. The almost homogeneous distribution exhibited by Si is related to its high diffusivity in aluminum, allowing it to dissolve more easily into the matrix during the laser melting process. In fact, due to its smaller atomic size and good solubility, Si diffuses more rapidly, contributing to the formation of solid solutions. On the other hand, the Fe distribution map clearly demonstrates its irregular distribution, likely due to incomplete mixing with the α-Al matrix, despite the presence of a turbulent flow. The diffusive motion of Fe appears to have been frozen by the rapid solidification that characterized the PBF-LB/M process. This result was unexpected, considering that in the powder produced with IGA, a homogeneous composition was obtained (Figure 1). Interestingly, the observed inhomogeneity is reminiscent of findings from a similar study conducted by our research group, where AlSi10Mg was mechanically mixed with Cu [20]. In that case, the diffusive motion of Cu was similarly immobilized by the rapid solidification induced during the laser scan in SST production. However, this issue was successfully resolved when pre-alloyed powders obtained via the IGA process were employed [12], enabling a more uniform distribution of Cu throughout the matrix. In the present study, despite directly using AlFe18Si8Cr5Ni2 pre-alloyed powders, this inhomogeneity effect was still observed. A closer examination of the literature provides a possible explanation for this behavior. According to Lee et al. [21], Fe diffuses significantly more slowly in liquid Al than Cu, as demonstrated by comparative diffusion studies at temperatures above the equilibrium melting point of Al. Their findings, along with earlier experiments by Isono et al. [22] on supercooled Al alloys, suggest that Fe sluggish diffusion may be due to the formation of tightly bound clusters of 7–20 Al atoms around individual Fe atoms, as proposed by Turnbull [23]. These clusters reduce Fe mobility in the liquid phase. Furthermore, Fe is an inherently slow diffuser in solid Al. This behavior has been attributed to differences in valence, as Al has a valence of 3, while Fe dissolved in Al exhibits a lower valence of approximately 2.53 [24]. The valence disparity further hampers Fe diffusivity not only in the solid state but also in the liquid phase of Al [25]. As a result, even under the high temperatures and turbulent conditions of the PBF-LB/M process, Fe diffusion remains limited, leading to localized irregularities in its distribution.

Although the information on SSTs is useful for understanding the initial microstructural development, it remains limited in the context of the entire PBF-LB/M process. This is because SSTs represent only a small portion of the material, while the laser passes multiple times during the PBF-LB/M process, leading to more complex phenomena of heat accumulation and material interaction. To gain a more comprehensive understanding of AlFe18Si8Cr5Ni2 behavior under laser action, it is crucial to analyze the PBFed bulk sample, which provides insights into the cumulative effects of repeated laser scans and the resultant material properties. Analyzing the bulk sample allows for a more accurate representation of the final microstructure, capturing the full extent of the thermal gradients, forming solid solutions, and the evolution of phase distributions that occur throughout the entire build.

The SEM analyses in Figure 3 reveal that some residual cracks are still present in the sample. However, crack-free regions were selected to investigate the microstructural features of this alloy following the PBF-LB/M process. These observations, enabled by SEM analysis of the consolidated samples, also allow for direct comparison with the features previously identified in the powder. SEM-BSE images highlight the melt pool boundaries, distinguished by a brighter coarse acicular structure, suggesting compositional enrichment with heavier elements. Diffusive movements of Fe are no longer evident, as seen in the cross-sectioned SST (Figure 2). Instead, the melt pool boundaries exhibit coarse, bright acicular phases, contrasting sharply with the darker melt pool centers, which display finer, globular microstructural features (as highlighted in the high-magnification micrograph in Figure 3). To determine which element these coarse acicular regions are enriched with, low-magnification EDS mapping was performed (Figure 4).

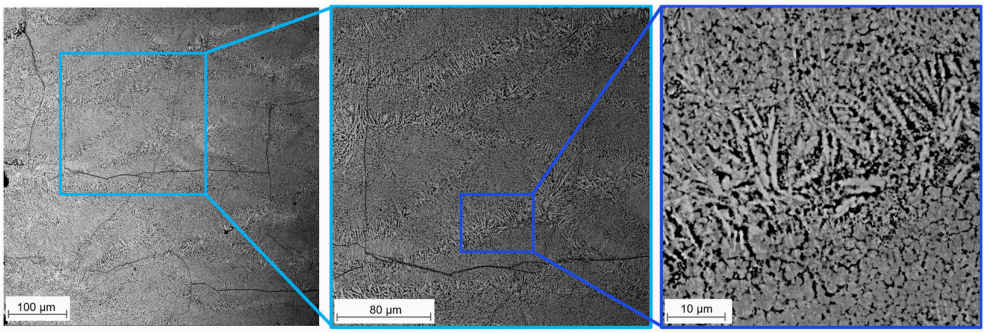


Figure 3. SEM-BSE micrographs of the PBFed AlFe18Si8Cr5Ni2 sample at three different magnifications.

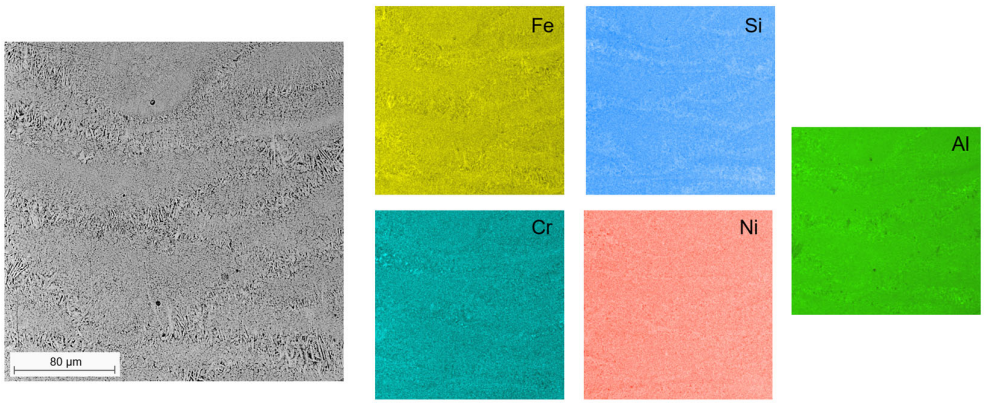


Figure 4. SEM-BSE micrograph and corresponding EDS maps illustrating the spatial distribution of primary alloying elements.

The EDS maps shown in Figure 4 clearly reveal that the coarse acicular features located at the melt pool boundaries in the bulk PBF-LB/M sample are enriched in Fe. This Fe-rich phase distribution is reminiscent of the chemical segregation observed at the melt pool

boundaries in the SST cross-section reported in Figure 2. While in SSTs Fe segregation followed distinct diffusion paths during solidification, which were effectively 'frozen' in the cross-section, highlighting the preferential presence of Fe towards the periphery of the melt pool, the complex thermal history associated with the layer-by-layer nature of the PBF-LB/M process significantly alters the solidification dynamics. However, even in the bulk sample, the boundaries of the melt pool (corresponding to the periphery of the SST cross-section) remain preferential sites for Fe segregation, as demonstrated by the presence of coarser acicular phases rich in Fe, confirmed by EDS analysis. This recurring localization of Fe-rich phases at melt pool boundaries should be explained by the limited diffusivity of Fe in Al due to its larger atomic radius and poor solubility [26]. It is likely that Fe atoms, rejected at the solidification front, accumulate at the last-to-solidify regions, i.e., the melt pool boundaries. The repeated thermal exposure in the PBF-LB/M process may further promote coarsening of these Fe-rich phases without enabling significant redistribution, thus preserving their preferential localization. These observations highlight a consistent segregation mechanism driven by thermodynamic and kinetic constraints, despite the differences in thermal history between SSTs and bulk samples. Additionally, these acicular features appear to be simultaneously depleted in silicon and aluminum. Notably, similar acicular phases were previously observed in the microstructure of the powders of this composition [12], where they also revealed an enrichment of Fe at the expense of Al and Si. This consistency suggests that these phases are inherent to the alloy chemistry and processing, persisting through the transition from powder to solidified structure after the PBF-LB/M process. Examining the less prevalent elements in the alloy reveals that Cr partially follows the distribution of Fe, predominantly localizing at the melt pool boundaries. However, certain regions exhibit a more pronounced segregation of Cr, forming distinct concentration zones. Notably, these Cr-rich areas coincide with triple points where multiple scan tracks overlap, suggesting a localized accumulation of this element in regions subjected to complex thermal histories. In contrast, Ni appears to be more uniformly distributed across the microstructure, with no significant enrichment at the melt pool boundaries. However, small, well-defined Ni-rich spots are distinguishable. Interestingly, these Ni-enriched regions coincide with localized enrichments of Al and Cr, suggesting the possible formation of phases incorporating these three elements. However, at this stage, the exact stoichiometry of these phases remains undetermined, necessitating further, more detailed compositional analysis to confirm their precise elemental makeup.

Then, to further investigate the morphology of the phases present within the melt pool, high-magnification analyses were performed using FESEM specifically in these regions (Figure 5). This approach provided a more detailed visualization of the microstructural features, allowing for a clearer differentiation between the fine, globular structures observed in the melt pool center and the coarser, acicular phases concentrated along the melt pool boundaries. In addition, these high-resolution images enabled a deeper understanding of the spatial arrangement, size, and shape of the phases.

These more detailed analyses revealed that the finer microstructure initially observed in Figure 3 at the melt pool center is of a dual nature; one component consists of simpler acicular phases arranged in star-like, interconnected patterns (reported in purple in Figure 5), while the other comprises globular features (reported in blue in Figure 5). Within the globular region, BSE imaging highlighted sub-micrometer-scale inhomogeneities, with distinct brighter areas indicative of higher-atomic-weight elements. These brighter zones appear to trace linear paths along multiple globular features, suggesting subtle segregation or clustering of heavier elements along specific directions. This intricate distribution of phases and compositional variations within the melt pool center provides valuable insights

into the complex interplay of solidification dynamics and element redistribution during the PBF-LB/M process.

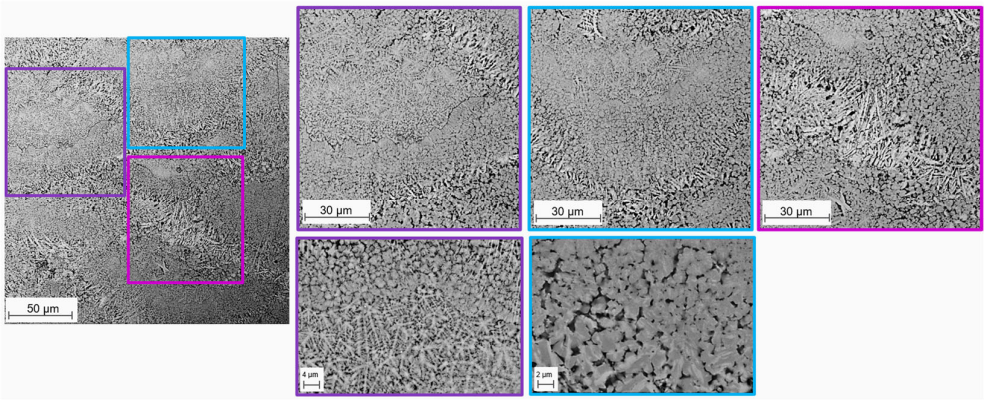


Figure 5. FESEM micrograph with high-magnification images of selected regions. The simpler acicular phases, arranged in star-like, interconnected patterns, are presented in purple, while globular features are shown in blue; both are predominantly located at the center of the melt pool. Acicular features characteristic of the melt pool boundary are depicted in pink.

3.2. Phase Identification Through XRD and Thermal Analysis

The XRD analysis was conducted to evaluate the effect of laser processing on the presence and amount of intermetallic phases in the bulk sample compared to those in the starting powder. The corresponding spectra are shown in Figure 6.

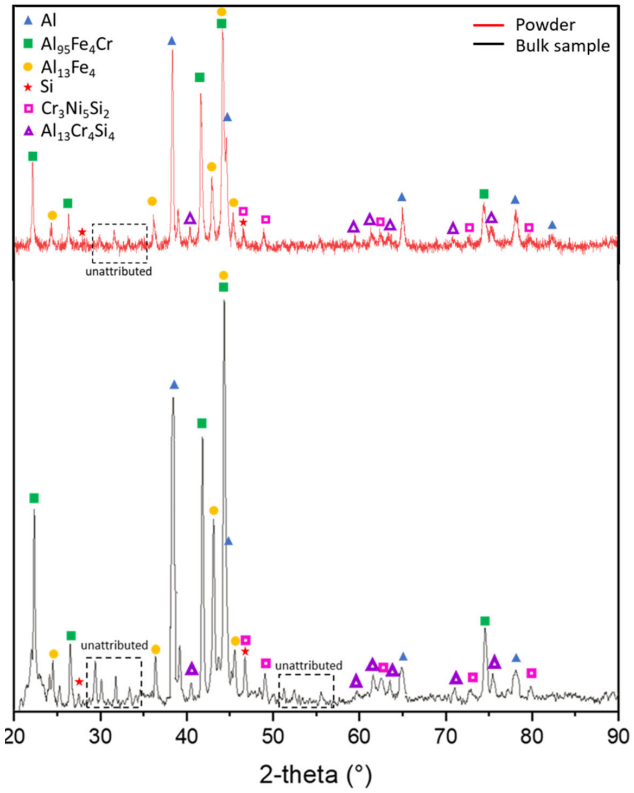


Figure 6. Powder and bulk X-ray diffraction patterns of AlFe18Si8Cr5Ni2.

The spectra reveal that the most intense peaks associated with the fcc-Al matrix remain unchanged after laser processing, indicating that the aluminum matrix is largely stable during the AM process. Additionally, peaks that in the powder spectrum were attributed to two intermetallic phases, $Al_{95}Fe_4Cr$ and $Al_{13}Fe_4$, are still present in the spectrum related

to PBFed material. However, after laser exposure, the $Al_{95}Fe_4Cr$ peaks appear more intense than in the starting powders, suggesting that the repeated thermal cycles inherent in the layer-by-layer process promote the growth of this phase. This increase may be due to the enhanced diffusion of Fe and Cr atoms at elevated temperatures, which favors the precipitation and stabilization of $Al_{95}Fe_4Cr$ over multiple heating and cooling cycles.

Furthermore, the pure Si peaks, although still visible, exhibit a significant reduction in intensity, suggesting that laser processing facilitates chemical reactions between Si and other elements, particularly Al, Cr, and Ni. These interactions likely lead to the formation of additional intermetallic phases, specifically $Cr_3Ni_5Si_2$ and $Al_{13}Cr_4Si_4$. While these phases were already detected in the starting powders, their presence in the bulk material is noticeably more pronounced. The transformation probably occurs due to the increased solubility of Si in the Al-rich matrix at high temperatures, which then reacts with Cr and Ni upon solidification.

Additionally, peaks detected in the 29–35° range of the AlFe18Si8Cr5Ni2 powder appear more intense in the bulk spectrum. However, due to the high signal noise and the overlapping of multiple peaks associated with Al-Fe and Al-Fe-Si-containing phases in this range, unambiguous phase identification was not possible. Nevertheless, the increased intensity of these peaks, along with the emergence of new peaks in the 50–60° range that were absent in the powder, suggest that the higher thermal energy input and the layer-by-layer nature of the PBF-LB/M process accelerate phase transformation kinetics. The prolonged exposure to elevated temperatures and the repeated melting and rapid solidification events may have facilitated further nucleation and growth of intermetallic compounds, increasing their content beyond 1 wt% and so making them detectable via XRD.

These phase transformations between the raw powder and the PBF-LB/M bulk material, as observed in the XRD analysis, indicate significant microstructural evolution during laser processing, particularly in altering phase stability and distribution within the material. To further assess the effect of the laser and the PBF-LB/M process on the material, DSC analysis was conducted as a complementary approach to investigate thermal stability and phase transitions (Figure 7). The DSC experiments were carried out up to the complete melting of the sample, including a slow cooling ramp to simulate solidification under near-equilibrium conditions.

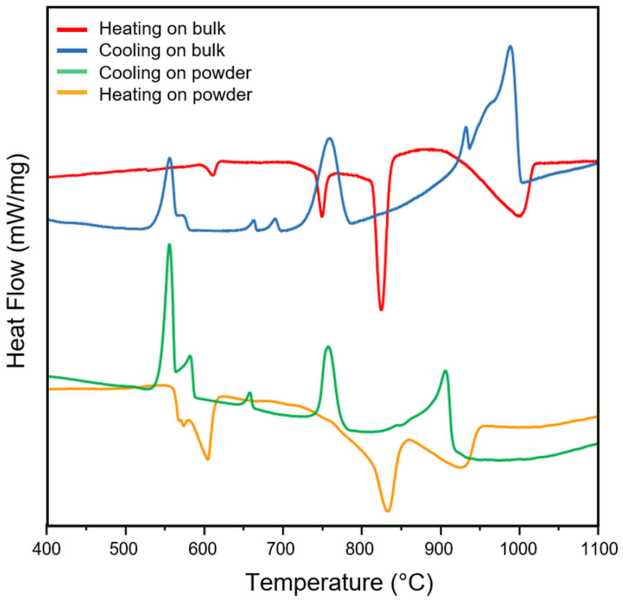


Figure 7. DSC analyses of AlFe18Si8Cr5Ni2 powder and PBFed bulk sample.

Starting with examining the heating curves of both the starting powder and the PBFed bulk sample, it is possible to observe several endothermic peaks. The endothermic nature of the peaks indicates phase dissolution or melting processes that require energy. The presence of these peaks in the DSC diagram confirms that the corresponding phases were present in the initial material, either in the powder after the rapid solidification during IGA or in the bulk material after the extremely fast solidification and remelting characteristic of the PBF-LB/M process. In the heating DSC pattern of the starting powder, the first notable feature is a double peak centered at approximately 580 and 600 °C. According to Han et al. [27] and Bhatt et al. [11], based on the Gulliver–Scheil model, the first peak can be attributed to the main eutectic reaction with the dissolution of the $Al_{13}Fe_4$ phase (often referred to in the literature as Al_3Fe), which is consistent with the XRD findings (Figure 6). The second peak likely corresponds to the melting of α-Al, potentially overlapping with the fusion of the $Al_{95}Fe_4Cr$ phase. Additionally, a pronounced third peak appears around 825 °C, followed by a broader, less intense peak near 920 °C. Based on Tang et al. [28], these peaks could be associated with the melting of primary Si or transformation related to $Cr_3Ni_5Si_2$ phase, which was also detected in the XRD analysis.

Moving to the heating curve analysis of the PBFed sample, at approximately 600 °C, where the double peak was observed in the powder curve, only the higher-temperature peak remains. This feature corresponds to the melting of α-Al, potentially overlapping with the formation of the $Al_{95}Fe_4Cr$ phase. The absence of the lower-temperature peak suggests that the repeated thermal cycling during PBF-LB/M processing has suppressed the formation of certain metastable phases or altered their transformation pathways, further emphasizing the strong impact of processing conditions on phase stability and microstructural evolution. In addition, with respect to the powder heating curve, a new endothermic peak appears around 750 °C. The latter could indicate the formation of metastable phases or compositional redistributions occurring during the repeated thermal cycling inherent to the PBF-LB/M process. Instead, the peak at approximately 825 °C, observed also in the powder curve, remains present in the bulk PBFed sample even if it appears narrower and more pronounced. Lastly, the broad peak observed in the powder near 920 °C is probably incorporated into a much larger, more energy-intensive peak extending up to 980 °C in the bulk sample curve. The amplification of the original peaks implies that the corresponding phases are present in a greater quantity or exhibit enhanced thermal stability due to changes in their morphology, distribution, or interactions with the surrounding matrix. The broadening and shift of the high-temperature endothermic peak towards 980 °C suggest that high-melting phases, such as $Cr_3Ni_5Si_2$, have undergone structural coarsening or stabilization due to extended exposure to elevated temperatures during processing. The increased energy demand for phase transformations in the bulk material further indicates a reduction in solute segregation compared to the as-atomized powder, potentially leading to the formation of more chemically homogeneous and thermally stable phases.

To better understand the nature of the phases undergoing endothermic reactions during the heating ramp, and, in particular, to determine whether they are stable or metastable and to assess the influence of the rapid solidification involved in the IGA or in the PBF-LB/M processes, slow cooling ramps were conducted. These controlled cooling experiments simulate phase formation under conditions closer to thermodynamic equilibrium, allowing for more precise evaluation of phase stability and transformation pathways. By comparing the thermal events observed during heating and cooling, insights can be gained into the effect of processing history on phase evolution, helping to distinguish between phases that are retained due to kinetic constraints and those that would naturally form under equilibrium solidification conditions. Analyzing the enthalpy variations during the controlled cooling ramp of the powder, which was first brought to complete melting, a

first exothermic peak is observed slightly above 900 °C, corresponding to the crystallization of primary Si. However, a pronounced tail extending to lower temperatures suggests the possible precipitation of phases like $Cr_3Ni_5Si_2$. Another exothermic peak appears at 770 °C, likely corresponding to phases that were seen dissolving around 820 °C during heating. The observed decrease in temperature may be due to the slower cooling rate, which could have facilitated the formation of high-melting phases, such as Si and $Cr_3Ni_5Si_2$, thereby depleting free Si in the molten bath and lowering the crystallization temperature. Before the expected crystallization of the $Al_{13}Fe_4$ phase, followed by α-Al or $Al_{95}Fe_4Cr$ between 550 and 600 °C, a minor exothermic peak is detected around 650 °C. Because this feature does not correspond to any dissolution peak in the heating ramp, it may be associated with an equilibrium phase that did not form in the powder due to kinetic constraints. The presence of this peak suggests that certain phases, which are suppressed under the rapid solidification conditions of IGA, become thermodynamically favored when sufficient time is allowed for atomic rearrangement during slow cooling.

In the controlled cooling ramp of the PBFed bulk sample, the first exothermic peak appears around 1000 °C, which is significantly higher than the primary crystallization event observed in the powder curve. The increased crystallization temperature compared to the powders indicates a possible stabilization of high-temperature phases in the bulk material. Similarly to the corresponding endothermic peak detected in the heating ramp, this exothermic reaction is accompanied by a broad tail extending towards lower temperatures, suggesting a gradual phase transformation or the sequential precipitation of multiple phases. Moving more specifically to the tail of the main peak, a secondary peak near 920 °C is observed, which roughly coincides with the peak observed in the cooling curve of the powder. A second exothermic peak is observed at 760 °C, which is likely associated with the crystallization of a phase that was seen melting at approximately 820 °C during heating. The downward shift of the crystallization peak during cooling, compared to the dissolution temperature during heating, can be attributed to the effects of solidification kinetics. The slower cooling rate promotes the segregation of solute elements and the formation of high-melting compounds, thereby reducing the amount of available low-melting constituents in the remaining liquid phase and lowering the crystallization temperature. Two additional minor exothermic peaks appear at 670 and 690 °C. The one at a lower temperature was already observed in the powder curve, contrarily to the one that occurred at a higher temperature. This newly formed peak suggests the presence of a stable phase that did not form in the powder. The appearance of this phase exclusively in the bulk material indicates that the thermal cycles of the PBF-LB/M process may have facilitated its formation, either by promoting elemental diffusion or by enabling the transformation of metastable phases into their stable counterparts. Around 600 °C, the characteristic double peak is observed, corresponding to the crystallization of the $Al_{13}Fe_4$ phase, followed by α-Al or $Al_{95}Fe_4Cr$. The appearance of this double peak, in contrast to the single broad peak observed during heating, suggests again that the PBF-LB/M process significantly altered phase formation kinetics. However, when subjected to slow and controlled cooling, the material returns to a phase formation behavior more similar to equilibrium conditions, resembling what was observed in the powder. This indicates that the phases formed during the rapid solidification of PBF-LB/M are strongly dependent on kinetic factors, with certain metastable phases potentially transforming into equilibrium phases under slower cooling conditions.

3.3. AlFe18Si8Cr5Ni2 Nanoscale Mechanical Properties Associated with the Microstructure

The heterogeneous microstructure observed in previous microstructural analyses, together with the large-scale thermal gradients to which the material is subjected during the

additive process and the stochastic nature of the defects, are factors that can significantly affect the macroscopic mechanical properties and, consequently, the ultimate applicability of the alloy studied. To fully explore the multiscale mechanisms contributing cooperatively to the alloy performance, a preliminary micromechanical–microstructural correlation study was conducted. This study involved high-resolution nano-hardness mapping overlaid on low-magnification BSE images and EDS maps for the PBFed AlFe18Si8Cr5Ni2 alloy (Figure 8).

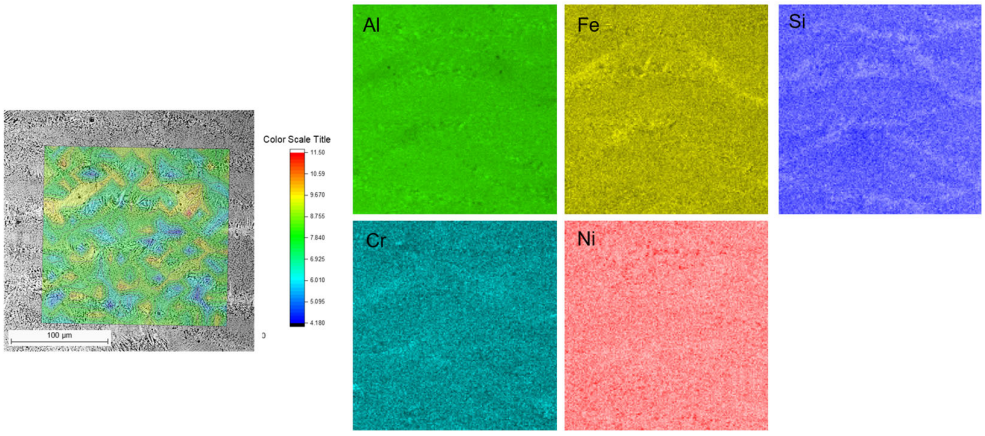


Figure 8. Overlay of BSE micrograph and nanoindentation hardness map with correlated EDS elemental maps, highlighting local mechanical properties and compositional variations.

As evident from Figure 8, the hardness map covers an area spanning at least six different melt pools. Notably, in some melt pools, the hardness distribution strongly correlates with the heterogeneous microstructure of the material. Due to the stripe scanning strategy with a 67° rotation used in the PBF-LB/M process, the melt pools captured in the hardness map represent polar cross-sections of three-dimensional pools, each with a unique hardness distribution. Overall, a significant variation in hardness is observed across the map, ranging from 4.2 to 11.5 GPa. Disproportionately high hardness values between 10 and 11.5 GPa are concentrated in specific melt pool boundary regions. These harder areas coincide with fine, compact acicular phases, which, when compared with EDS maps, correspond to Fe- and Cr-rich regions with a depletion of Si. However, melt pool boundaries featuring coarser, more widely spaced acicular phases rich in Fe do not exhibit the same hardness increase. This discrepancy can be attributed to the distinct thermal histories of different melt pools. Likely, these coarser phases experienced post-solidification thermal cycles from subsequent scan tracks, providing insufficient heat to induce remelting but promoting excessive aging, grain growth, and phase coarsening, ultimately reducing local hardness. In the central melt pool region, characterized by a diverse microstructure comprising globular features and simpler acicular phases arranged in star-like interconnected patterns, the hardness is generally lower. This can be attributed to a more uniform elemental distribution and a relative scarcity of hardening Al-Fe phases. These Al-Fe hardening phases solidify between 900 and 600 °C, well above the melting temperature of pure Al. Fe-rich Al phases begin nucleating at the melt pool boundaries, with their solidification following the Gaussian temperature profile. While these particles remain suspended in the liquid Al pool above 650 °C, Marangoni eddies transport a small fraction towards the top of the melt pool, with some particles becoming trapped in the interior due to growth competition. This results in intermittent high-hardness responses in the pool interior. However, because only a small fraction migrates to the melt pool center, the overall hardness remains lower than at the boundaries. Finally, Ni-rich spots identified in the EDS maps do not appear to correlate with localized hardness increases. This is likely

due to the spacing between nanoindentations and the extremely small size of the Ni-rich features, preventing their effective detection in the nanoindentation measurements.

From the nanoindentation tests, it was also possible to determine the reduced Young's modulus from the measured elastic stiffness ($S = \partial P/\partial h$) during the unloading stage. By applying Equation (1), E of the AlFe18Si8Cr5Ni2 alloy was calculated, yielding an average value of 163.8 GPa, with a 95% confidence interval of ±1.6 GPa. This result suggests a significant increase in stiffness compared to the base AlSi10Mg alloy, which typically exhibits a Young's modulus of around 73 GPa [29]. The measured modulus is, in fact, much closer to that of 304L stainless steel, which has a Young's modulus of approximately 193 GPa [30]. This behavior can be attributed to the complex multiphase microstructure identified by SEM, XRD, and DSC analyses, which revealed the presence of various intermetallic phases rich in Al, Fe, Cr, and Si. These phases contribute to the formation of a rigid and interconnected microstructural framework. The elevated modulus reflects the mechanical contribution of these hard intermetallic compounds, which are homogeneously distributed within the aluminum matrix and significantly enhance the overall elastic response of the alloy.

Although the measured Young's modulus indicates a significant increase in stiffness, suggesting a potentially more rigid mechanical response with the normal Al-based alloy behavior, this prompted further investigation into the plastic deformability of the AlFe18Si8Cr5Ni2 alloy. It is well-known that the elastoplastic properties of materials are key indicators of their mechanical performance and have guiding significance in materials science and engineering. In recent years, the nanoindentation technique has emerged as a powerful tool to probe the intrinsic elastoplastic response of materials at the micro scale [31]. One preliminary indication of the alloy plastic behavior can be obtained by examining the residual displacement after the unloading phase of the nanoindentation test. Figure 9 shows a representative P–h curve for the AlFe18Si8Cr5Ni2 alloy, which reflects the average mechanical response observed across multiple indents.

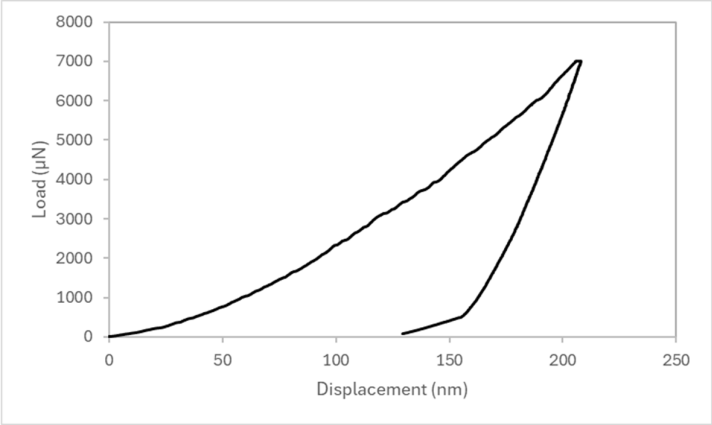


Figure 9. A representative P–h curve for the AlFe18Si8Cr5Ni2 alloy.

From the curve, it is evident that a significant residual depth remains after unloading, which is approximately 130 nm out of a total maximum penetration of 207 nm, indicating a substantial amount of plastic deformation. Applying Equation (2), it was possible to calculate Ψ for each indentation, obtaining 0.63 as the mean value. Based on Shakil et al.'s study [32], Ψ should range between 0 and 1, where Ψ = 0 corresponds to a fully elastic response, Ψ = 1 indicates fully plastic behavior, and intermediate values ($0 < \Psi < 1$) reflect an elastic–plastic deformation regime. The calculated plasticity index places the AlFe18Si8Cr5Ni2 alloy in a regime characterized by a predominantly plastic response while still retaining an elastic component. This relatively high value suggests that the material

undergoes significant permanent deformation under load, indicative of a good capacity to dissipate mechanical energy without immediate failure. Such behavior is consistent with materials that exhibit a combination of stiffness and ductility.

In addition, a particularly valuable metric in nanoindentation is the creep rate $\dot{\varepsilon}$, which describes the time-dependent plastic deformation under constant load. During the hold period of a nanoindentation, the tip continues to slowly penetrate the material as time progresses due to time-dependent deformation mechanisms active beneath the indenter. This process is sensitive to the material microstructure, including the presence and mobility of defects, such as dislocations, vacancies, and grain boundaries [33]. The $\dot{\varepsilon}$ reflects the material ability to accommodate deformation under sustained stress, and it was calculated following Equation (2). The creep rate was calculated over all hold segments of each indentation test, resulting in an average plateau value of 0.006 s^{-1}, with a 95% confidence interval of $\pm$0.003 s^{-1}. To contextualize this result, the measured average creep rate falls within an intermediate range when compared to typical values reported for Al-based alloys and 304L stainless steel [34,35]. This suggests that the AlFe18Si8Cr5Ni2 alloy exhibits a moderate viscoplastic response, reflecting a balance between stiff intermetallic phases and microstructural pathways that still allow for time-dependent plastic deformation.

Ultimately, the creep rate analysis combined with residual displacement data suggest that despite the alloy high stiffness, the material retains a notable level of plasticity, which is encouraging from the standpoint of mechanical performance and potential structural applications. However, to fully assess its suitability for engineering use, further investigations at the macro scale are required.

4. Conclusions

This study investigated the microstructural evolution and local mechanical properties of a novel AlFe18Si8Cr5Ni2 alloy processed via PBF-LB/M for the first time. The findings from this study can be summarized as follows.

- EDS analysis of cross-sectioned SSTs revealed Fe inhomogeneity due to its low diffusivity in Al, despite using pre-alloyed powders.
- Fe-rich acicular intermetallic phases were observed in both the powder and the PBFed material but with different distribution. In the powder, they are finer and uniformly dispersed, while in the bulk, they predominantly segregate along melt pool boundaries. The PBF-LB/M microstructure is more complex, featuring finer acicular phases that form star-like interconnected patterns and globular features at the melt pool center.
- EDS analysis showed that Fe-rich acicular phases in both powder and bulk are Si-depleted. Pure Si-rich spots were only observed in the powder. Cr and Ni distributions suggest more complex interactions; in the powder, Cr shows localized enrichments often associated with Si and Ni, while in the bulk, Cr and Ni tend to segregate at specific regions like melt pool boundaries and triple points, indicating phase formation influenced by thermal history.
- XRD and DSC analyses revealed significant modifications in the phase composition during laser processing with respect to the powder, with a notable increase in $Al_{95}Fe_4Cr$ content and the formation of high-melting intermetallic compounds, such as $Cr_3Ni_5Si_2$. The rapid thermal cycling of PBF-LB/M proved to alter phase stability, promoting phase growth and transformation kinetics.
- Nanoindentation mapping correlated local hardness variations with specific microstructural features, confirming that Fe- and Cr-rich phases at melt pool boundaries exhibited higher hardness values, while globular phases in the melt pool centers resulted in relatively lower hardness.

- Despite a stiffness of around 163.8 GPa, the alloy exhibits notable plasticity, as evidenced by a significant residual indentation depth (~130 nm out of 207 nm) and a measurable creep rate (0.006 s^{-1}), indicating its capacity for time-dependent viscoplastic deformation and suggesting promising mechanical performance for potential structural applications.

The study provided novel insights into the microstructural and phase evolution of this alloy under rapid solidification, particularly regarding the formation and persistence of Fe-rich acicular phases, the role of Cr and Ni in phase distribution, and thermal and mechanical behavior. These findings deepen the understanding of the influence of PBF-LB/M on the alloy behavior and contribute to advancing alloy design strategies for sustainable AM.

Author Contributions: Conceptualization, M.L. and P.F.; formal analysis, A.M.; investigation, A.M.; data curation, A.M.; writing—original draft preparation, A.M.; writing—review and editing, A.M. and M.L.; supervision, M.L. and P.F. All authors have read and agreed to the published version of the manuscript.

Funding: This research received no external funding.

Data Availability Statement: The raw data supporting the conclusions of this article will be made available by the authors upon request.

Acknowledgments: The authors would like to thank Federico Gobber and Enrico Virgillito for their support in the production of the powders used in this study.

Conflicts of Interest: The authors declare no conflicts of interest.

References

1. Song, D.; Zhao, Y.; Jia, Y.; Li, R.; Zhou, N.; Zheng, K.; Fu, Y.; Zhang, W. Study of the evolution mechanisms of Fe-rich phases in Al-Si-Fe alloys with Mn modification using synchrotron X-ray imaging. *J. Alloys Compd.* **2022**, *915*, 165378. [CrossRef]
2. Ning, W.; Zhang, W.; Zhao, Y. Phase-field simulation for evolution of iron-rich phase during solidification of Al–Si–Fe alloys. *J. Mater. Res. Technol.* **2024**, *29*, 5495–5506. [CrossRef]
3. Dash, S.S.; Chen, D. A Review on Processing–Microstructure–Property Relationships of Al-Si Alloys: Recent Advances in Deformation Behavior. *Metals* **2023**, *13*, 609. [CrossRef]
4. Seifeddine, S.; Johansson, S.; Svensson, I.L. The influence of cooling rate and manganese content on the β-Al5FeSi phase formation and mechanical properties of Al-Si-based alloys. *Mater. Sci. Eng. A* **2008**, *490*, 385–390. [CrossRef]
5. Petr, J. The Iron Correctors in Al-Si Alloys. *Int. J. Eng.* **2011**, *9*, 401–405.
6. Aranda, V.A.; Figueroa, I.A.; González, G.; García-Hinojosa, J.A.; Alfonso, I. Study of the microstructure and mechanical properties of Al-Si-Fe with additions of chromium by suction casting. *J. Alloys Compd.* **2021**, *853*, 157155. [CrossRef]
7. Elsharkawi, E.A.; MacNeil, D.; Chouraqui, B.; Chen, X.G. Exploring the Effect of Ni as an Impurity on Fe-Rich Phases in Simulated Direct Chill Casting Al–Fe-Si Alloys. *Metallogr. Microstruct. Anal.* **2022**, *11*, 724–735. [CrossRef]
8. Petrík, J. The application of Ni for improvement of Al-Si-Fe alloys. *Mater. Eng.* **2009**, *16*, 29–32.
9. Podprocká, R.; Bolibruchová, D. The role of manganese in the alloy based on Al-Si-Mg with higher iron content. *Manuf. Technol.* **2018**, *18*, 650–654. [CrossRef]
10. Lavernia, E.J.; Srivatsan, T.S. The rapid solidification processing of materials: Science, principles, technology, advances, and applications. *J. Mater. Sci.* **2010**, *45*, 287–325. [CrossRef]
11. Bhatt, B.; Martucci, A.; Virgillito, E.; Gobber, F.; Bondioli, F.; Manfredi, D.; Lombardi, M.; Fino, P. Deciphering Microstructures and Phases of Gas-Atomised Novel Al-Fe-Si-Cr-Ni Alloys. *Metals* **2024**, *14*, 17. [CrossRef]
12. Martucci, A.; Gobber, F.; Aversa, A.; Manfredi, D.; Fino, P.; Lombardi, M. Improvement in the PBF-LB/M processing of the Al-Si-Cu-Mg composition through the use of pre- alloyed powder Improvement in the PBF-LB/M processing of the Al-Si-Cu-Mg composition through the use of pre-alloyed powder. *Mater. Res. Express* **2023**, *10*, 046508. [CrossRef]
13. Yadegari, M.J.; Martucci, A.; Biamino, S.; Ugues, D.; Montanaro, L.; Fino, P.; Lombardi, M. Aluminum Laser Additive Manufacturing: A Review on Challenges and Opportunities Through the Lens of Sustainability. *Appl. Sci.* **2025**, *15*, 2221. [CrossRef]
14. Yang, H.; Sha, J.; Zhao, D.; He, F.; Ma, Z.; He, C.; Shi, C.; Zhao, N. Defects control of aluminum alloys and their composites fabricated via laser powder bed fusion: A review. *J. Mech. Work. Technol.* **2023**, *319*, 118064. [CrossRef]

15. Robinson, J.H.; Ashton, I.R.T.; Jones, E.; Fox, P.; Sutcliffe, C. The effect of hatch angle rotation on parts manufactured using selective laser melting. *Rapid Prototyp. J.* **2019**, *25*, 289–298. [CrossRef]
16. *ISO 14577*; Metallic Materials—Instrumented Indentation Test for Hardness and Materials Parameters. International Organization for Standardization: Geneva, Switzerland, 2015.
17. Oliver, W.C.; Pharr, G.M. An improved technique for determining hardness and elastic modulus using load and displacement sensing indentation experiments. *J. Mater. Res.* **1992**, *7*, 1564–1583. [CrossRef]
18. Yamamoto, M.; Tanaka, M.; Furukimi, O. Hardness–deformation energy relationship in metals and alloys: A comparative evaluation based on nanoindentation testing and thermodynamic consideration. *Materials* **2021**, *14*, 7217. [CrossRef]
19. Charitidis, C.A.; Dragatogiannis, D.A.; Koumoulos, E.P. A study on time dependent properties of aluminum alloy by nanoindentation technique. *Int. J. Struct. Integr.* **2013**, *4*, 33–54. [CrossRef]
20. Bosio, F.; Manfredi, D.; Lombardi, M. Homogenization of an Al alloy processed by laser powder bed fusion in-situ alloying. *J. Alloys Compd.* **2022**, *904*, 164079. [CrossRef]
21. Lee, N.; Cahoon, J. Interdiffusion of copper and iron in liquid aluminum. *J. Phase Equilibria Diffus.* **2011**, *32*, 226–234. [CrossRef]
22. Isono, N.; Smith, P.M.; Turnbull, D.; Aziz, M.J. Anomalous Diffusion of Fe in Liquid by the Pulsed Laser Technique AI Measured. *Metall. Mater. Trans. A* **1996**, *27*, 725–730. [CrossRef]
23. Turnbull, D. The Gram-Atomic Volumes of Alloys of Transition Metals with Al and Si. *Acta Met. Mater.* **1990**, *38*, 243–249. [CrossRef]
24. Burachynsky, V.; Cahoon, J.R. A Theory for Solute Impurity Diffusion, Which Considers Engel-Brewer Valences, Balancing the Fermi Energy Levels of Solvent and Solute, and Differences in Zero Point Energy. *Met. Mater. Trans. A* **1997**, *28*, 563–582. [CrossRef]
25. Cahoon, J.R.; Broughton, W.H.; Kutzak, A.R. The determination of yield strength from hardness measurements. *Metall. Trans.* **1971**, *2*, 1979–1983. [CrossRef]
26. Raghavan, V. Al-Fe-Si (Aluminum-Iron-Silicon). *J. Phase Equilibria Diffus.* **2012**, *33*, 322–326. [CrossRef]
27. Han, Y.; Ban, C.; Zhang, H.; Nagaumi, H.; Ba, Q.; Cui, J. Investigations on the solidification behavior of Al-Fe-Si alloy in an alternating magnetic field. *Mater. Trans.* **2006**, *47*, 2092–2098. [CrossRef]
28. Tang, J.; Jia, W.; Wang, Y.; Shi, Y.; Huang, H.; Zhang, G. Phase evolution and magnetic properties of rapidly solidified Si-substituted CoCrFeMnNi high entropy alloy. *J. Alloys Compd.* **2025**, *1010*, 177608. [CrossRef]
29. Serjouei, A.; Libura, T.; Brodecki, A.; Radziejewska, J.; Broniszewska, P.; Pawłowski, P.; Szymczak, T.; Bodaghi, M.; Kowalewski, Z. Strength-hardness relationship for AlSi10Mg alloy produced by laser powder bed fusion: An experimental study. *Mater. Sci. Eng. A* **2022**, *861*, 144345. [CrossRef]
30. Zhang, H.; Li, C.; Yao, G.; Zhang, Y. Hot isostatic pressing of laser powder-bed-fused 304L stainless steel under different temperatures. *Int. J. Mech. Sci.* **2022**, *226*, 107413. [CrossRef]
31. Long, X.; Dong, R.; Su, Y.; Chang, C. Critical Review of Nanoindentation-Based Numerical Methods for Evaluating Elastoplastic Material Properties. *Coatings* **2023**, *13*, 1334. [CrossRef]
32. Shakil, S.I.; Hadadzadeh, A.; Amirkhiz, B.S.; Pirgazi, H.; Mohammadi, M.; Haghshenas, M. Additive manufactured versus cast AlSi10Mg alloy: Microstructure and micromechanics. *Results Mater.* **2021**, *10*, 100178. [CrossRef]
33. Golovin, Y.I. Nanoindentation and Mechanical Properties of Materials at Submicro- and Nanoscale Levels: Recent Results and Achievements. *Phys. Solid State* **2021**, *63*, 1–41. [CrossRef]
34. Shakil, S.I.; Hadadzadeh, A.; Pirgazi, H.; Mohammadi, M.; Haghshenas, M. Indentation-derived creep response of cast and laser powder bed fused AlSi10Mg alloy: Air temperature. *Micron* **2021**, *150*, 103145. [CrossRef] [PubMed]
35. Khan, S.; Junaid, M.; Khan, F.N. Nanoindentation and indentation creep analysis of diffusion bonded of inconel 718 and AISI 304L stainless steel joint interface. *Proc. Inst. Mech. Eng. Part L J. Mater. Des. Appl.* **2024**. [CrossRef]

Disclaimer/Publisher's Note: The statements, opinions and data contained in all publications are solely those of the individual author(s) and contributor(s) and not of MDPI and/or the editor(s). MDPI and/or the editor(s) disclaim responsibility for any injury to people or property resulting from any ideas, methods, instructions or products referred to in the content.